Intermetallics 185 (2025) 108897

Contents lists available at ScienceDirect

Intermetallics

journal homepage: www.elsevier.com/locate/intermet

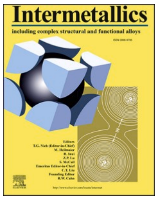

Improvement of corrosion-wear resistance of Zr-based metallic glass by pre-oxidation treatment

Yu Zhang [a,b], Wenxue Wang [b], Yong Xiao [a], Jiang Ma [b,*]

[a] School of Materials Science and Engineering, Wuhan University of Technology, Wuhan, 430070, China
[b] Shenzhen Key Laboratory of High Performance Nontraditional Manufacturing, College of Mechatronics and Control Engineering, Shenzhen University, Shenzhen, 518060, China

ARTICLE INFO

Keywords:
Metallic glasses
Wear resistance
Corrosive environment
Pre-oxidation treatment

ABSTRACT

Zr-based bulk metallic glasses (BMGs) are considered to have broad application prospects due to their superior mechanical properties and excellent glass forming ability (GFA). However, the wear resistance of Zr-based BMGs, especially when exposed to corrosive liquid environments, is insufficient and could decrease their service reliability in special environments. Here, we report a facile method that can significantly enhance the corrosion-wear performance of Zr-based MBGs, termed as pre-oxidation treatment (PT). The key parameters of electrochemical experiments proved that PT samples have a lower tendency to corrosion, the wear rates of the PT samples in 3.5 % NaCl neutral solution and 1N HCl acidic solution were 1.55×10^{-6} mm^3 N^{-1} m^{-1} and 0.88×10^{-6} mm^3 N^{-1} m^{-1}, respectively, which are significantly lower than those of the As-cast (AC) samples (29.8×10^{-6} mm^3 N^{-1} m^{-1} and 44.99×10^{-6} mm^3 N^{-1} m^{-1}, respectively). AC and PT samples both experienced synergistic effects of corrosion and mechanical wear, AC samples primarily experienced abrasive, adhesive, fatigue, and minor oxidative wear with corrosive wear. PT samples, with a high-hardness oxide layer, the wear debris and corrosion products could form lubrication, shown better resistance to mechanical wear, making mild abrasive and corrosive wear their main wear mechanisms. Our results demonstrates that PT can significantly enhance the corrosion-wear durability of metallic glasses, thereby unlocking engineering potential in corrosive-service environments.

1. Introduction

Bulk metallic glasses (BMGs) are a novel material that has emerged in recent decades [1,2], the unique long-range disordered structure endows it outstanding physical and chemical properties [3,4], manifested in larger elastic limit [5], exceptional strength [6,7], excellent catalystic performance and good wear resistance [8,9]. Among them, Zr-based metallic glass is renowned for its high glass-forming ability (GFA), for example, Qiao et al. [10] proved that the critical dimensions of Zr-based metallic glass can be over 20 mm, simultaneously, the manufacturing cost compared with other precious metal-based BMGs with the same GFA is much lower [11], which makes them promising applications for engineering materials. So far, they have already been used for making golf club heads, solar wind collectors for aerospace, mobile phone covers, and precision parts [12–15].

In practical applications such as food processing, ocean exploration, biomedical, and chemical industries, the sliding motion of materials exposed to corrosive environments is inevitable. Ji et al. [16] studied the wear of $Cu_{42}Zr_{47}Ag_4$ metallic glass (MG) in simulated seawater 3.5 % NaCl solution, the results showed that the main wear mechanism of the alloy was a combination of abrasive wear and corrosive wear. Meanwhile, through the calculation of wear mass loss, it was found that the MG 20 times exceeded AISI 304 stainless steel in terms of corrosion and wear resistance. Zr-based MGs become potential candidate materials for applications under severe corrosion and wear conditions due to the mentioned excellent corrosion and wear resistance, but the degree of wear damage exacerbated by corrosive environments is inevitable. Wang et al. [17] investigated the corrosion-wear behavior of $Zr_{61}Ti_2Cu_{25}Al_{12}$ MG under deionized water cooling and lubrication conditions, the damage caused by abrasive wear was mitigated compared to dry friction conditions. However, in a chloride-ion-containing corrosive environment, the wear situation was exacerbated due to the breakdown of the passivation film, with the wear process predominantly governed by the synergistic effects of abrasive wear and corrosion-induced wear.

---

* Corresponding author.
E-mail address: majiang@szu.edu.cn (J. Ma).

https://doi.org/10.1016/j.intermet.2025.108897
Received 10 May 2025; Received in revised form 10 June 2025; Accepted 22 June 2025

Consequently, it is imperative to explore effective strategies for enhancing the wear resistance of Zr-based MGs in corrosive solutions, thereby facilitating their broader application across various fields.

To improve the synergistic effect of abrasive and corrosive wear, it is essential to enhance both the wear and corrosion resistance of Zr-based MGs. Zhang et al. [18] reported that the oxidation treatment can affect the surface hardness and modulus of Zr-based MG, the improved mechanical properties are usually related to the wear resistance of materials. Salehan et al. [19] investigated the effect of different temperature-annealing on the wear behavior of $Zr_{60}Cu_{10}Al_{15}Ni_{15}$ MG, results indicate that the structure relaxed sample after annealing treatment exhibits the best wear resistance, and the wear resistance of the material is closely related to the dominant wear mechanism during the wear process. Nie et al. [20] reported that the ZrO_2-enriched but Cu-depleted nanostructured oxide film formed in $Zr_{64}Cu_{16}Ni_{10}Al_{10}$ could significantly improve the passivity in 0.5 M NaCl. Based on the above results, Pre-oxidation treatment (PT), as a facile and economical way, shows improvements in both wear and corrosion resistance. So the performance of corrosive wear resistance of oxidized Zr-based MG is anticipated, but this kind of researches remains insufficient.

In this work, a thickness of 1.23 μm oxide film was prepared on the surface of $Zr_{55}Cu_{30}Ni_5Al_{10}$ MG through PT, the thin film significantly enhanced both the corrosion resistance and wear resistance of Zr-based MG in 3.5 % NaCl and 1N HCl solutions. Specifically, the higher open circuit potential and wider passivation zone indicate lower corrosion tendency in PT sample. The wear rates of PT specimen measured 1.55×10^{-6} mm^3 N^{-1} m^{-1} in neutral 3.5 % NaCl solution and 0.88×10^{-6} mm^3 N^{-1} m^{-1} in acidic 1N HCl solution, exhibiting substantial reductions compared to As-cast (AC) sample. Mechanism analysis revealed that both AC and PT specimens experienced a synergistic effect of corrosion and mechanical wear during corrosive wear testing. For AC sample, the wear mechanism mainly manifests as abrasive wear accompanied by corrosive wear, adhesive wear, fatigue wear, and slight oxidative wear. However, the PT samples have a higher surface hardness oxide layer, which enhances their ability to resist mechanical wear, while wear debris and corrosion products generated during the process demonstrate lubricating effects, collectively decreasing wear severity. So the main wear mechanisms for PT specimens in the above-mentioned corrosive solution are slight abrasive wear and corrosive wear. Our results emphasize that PT demonstrates a marked capacity to enhance the corrosive wear resistance of MGs, positioning it as a promising candidate for an advanced method to improve the corrosion and wear performance of metallic materials.

2. Experimental method

2.1. Sample preparation

The Zr-based MG composition used in this study is $Zr_{55}Cu_{30}Ni_5Al_{10}$ (at.%), mainly because its good glass forming ability and wide supercooled liquid region, it was prepared through vacuum arc melting under purity over 99.99 % (4N) argon gas shielding. The purity of raw metal materials of each element exceeds 99.99 (wt.%) to minimize the tendency towards crystallization as much as possible. During the fabrication, the master alloy was melted roughly 5 times to ensure the uniform distribution of the elements, then the molten alloy was cast into a copper mold then fabricated 1.5 mm × 20 mm × 50 mm MG plate. The plate was then cut into an 11 mm disk by speed wire electrical discharge machining (WEDM, SODICK AP250L), with a positioning notch on it, as demonstrated in Fig. 1d. The PT was conducted in a tubular annealing furnace, set temperature as 380 K, hold at temperature for 90 min under an air atmosphere.

2.2. Structural characterization

The amorphous property of AC MG was analyzed by Cu-Kα radiation X-ray diffraction (XRD, Rigaku, MiniFlex 600), the wavelength of the X-ray is 0.154 nm, and the rated power is 600 W, the scan angle is from 20° to 80°. The thermal response and characteristic temperature of this Zr-based MG were analyzed by differential scanning calorimetry (DSC, PerkinElmer, DSC- 8000), with the scan rate was set as 20 K/min. The thickness of oxide film, the surface micro-structure after wear test, and

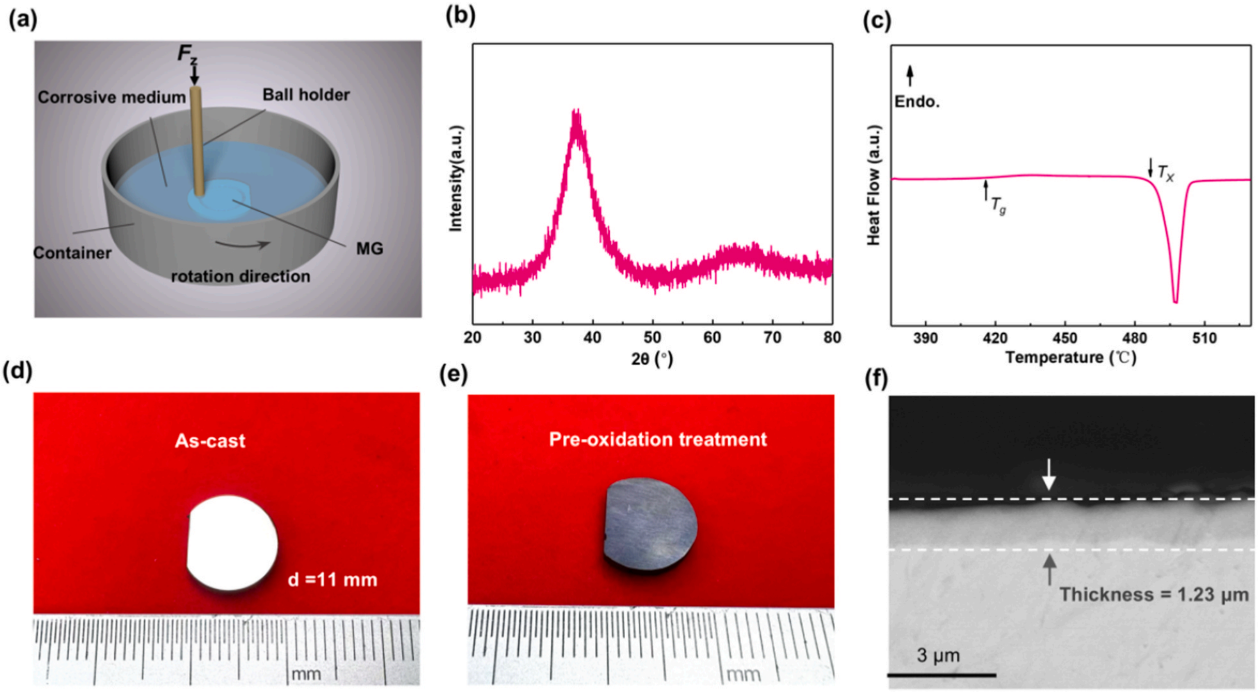

Fig. 1. (a) A schematic diagram of the corrosion-wear experiment. (b) X-ray pattern of $Zr_{55}Cu_{30}Ni_5Al_{10}$ metallic glass disk. (c) DSC trace and characteristic temperature of $Zr_{55}Cu_{30}Ni_5Al_{10}$ MG. (d) A photo of the As-cast (AC) sample with a positioning notch. (e) A photo of a pre-oxidation treatment (PT) sample with a positioning notch. (f) A Backscattering morphology from the cross-section of the PT sample.

corresponding elemental distribution were analyzed by a field emission scanning electron microscope (SEM, FEI, QUANTA FEG 450) with energy dispersive spectroscopy (EDS) capability. The morphology and the volume loss after the wear experiment were analyzed by a white light interference profiler (Bruker, Contour, GT-X 3D). Formation of surface substances on Zr-based MG after wear test was detected by X-ray photoelectron spectroscopy (XPS, Thermo Scientific, K-Alpha), charge correction was performed by using the C 1s peak (assigned with a binding energy of 284.8 eV) as the reference standard. Subsequently, peak deconvolution fitting and chemical state identification analyses were conducted on the data by using Avantage software.

2.3. *Electrochemical test*

Electrochemical corrosion tests were conducted using an electrochemical workstation (HuaChen, CHI 660E, China) under a standard three-electrode configuration, the photo of this device is shown in Fig. S1. The corrosion behaviors of AC and PT Zr-based MG samples were tested in simulated seawater 3.5 % NaCl and 1 N HCl solutions. Specimens with a 5 mm diameter were used as the working electrodes, a platinum plate was used as the counter electrode, and an Ag/AgCl reference electrode was used to measure open-circuit potential and potentiodynamic polarization curves.

2.4. *Wear test*

To investigate the effects of PT on the corrosion-wear of Zr-based MG samples, the wear test was conducted on a multifunctional tribometer (RTEC, MFT-5000, USA), experiments used a ball-on-disk rotational wear configuration, with a 9.5 mm-diameter ZrO_2 ceramic ball as the counterface material, the hardness of the ball is about 14 GPa. The key wear parameters were set as follows: rotational speed of 100 rpm, applied load of 3.5 N, wear track radius of 3 mm, and total test duration of 30 min. Apart from the original test environment, a container filled with solutions as a corrosive medium during the test, the detailed schematic diagram can be seen in Fig. 1a. The wear rate ω can be calculated by the following equation [21,22]:

$$\omega = \frac{V_{loss}}{P*L} \tag{1}$$

Where V_{loss} is the total wear volume loss (mm^3); P is the applied normal load, set as 3.5 N in this test; L is the total sliding distance.

3. Results and discussions

3.1. *Pre-oxidation treatment of the sample*

The XRD pattern of the prepared MG disk is shown in Fig. 1b, it is a broad diffraction peak without any sharp peaks, indicating that the structure of the prepared MG disk is fully amorphous. Fig. 1c is the DSC curve of this MG, which reveals two characteristic temperatures, one is the glass transition (T_g) about 419 °C, another is the crystallization temperature (T_x) about 479 °C. According to the reported thermogravimetric analysis (TGA) data [23], the weight of the MG of the same composition starts to increase at about 380 °C while heating, which means that the oxidation film starts to form at this temperature. Considering the requirement to obtain a thicker oxide film as much as possible while avoiding crystallization, the temperature and duration are set as 380 °C and 90 min, respectively. Fig. 1e is the photo of MG after PT, the surface appears black due to the formation of oxide, the thickness of this oxide film is about 1.23 μm, which can be confirmed by the morphology from the cross-sectional images in Fig. 1f.

3.2. *Analysis of electrochemical corrosion behavior*

The open circuit potential (OCP) of AC and PT sample in NaCl solution is shown in Fig. 2a, two samples reached a steady-state potential after prolonged immersion, the stabilized OCP values are −0.38 V and −0.42 V belong to AC and PT, respectively, the much higher OCP value of PT sample indicates that it has better corrosion thermodynamic stability and exhibits lower corrosion tendency [24,25]. Fig. 2b reveals the potentiodynamic polarization curve of these two samples, the curves show that all samples undergo activation, passivation, and corrosion processes [26]. The detailed parameters of the polarization curve are displayed in Table 1. The PT sample shows higher E_{corr} than AC sample, usually, the higher the self-corrosion potential (E_{corr}) represents the less likely a material is to lose electrons, the lower its tendency to corrode [27,28]. The pitting potentials (E_{nit}) of the AC and PT samples are 0.026 V and 0.081 V, and the width of the passivation zone (ΔE) is 0.556 V and 0.558 V, respectively, although the pitting potential of the PT samples is relatively high, the passivation interval width of the two samples is almost the same, indicating that the performance of passivation film of the two samples is similar, both have good stability [29]. In conclusion, PT can increase the corrosion resistance of the sample, mainly manifested in a reduce occurrence trend of corrosion reactions. The surface micro-topography after potentiodynamic polarization treatment is shown in Fig. S2, the AC sample shows denser corrosion pores and a large amount of corrosion products, which corresponds to the results of the electrochemical test.

In addition to neutral solutions, the corrosion behavior of AC and PT samples under acidic conditions study also studied. Fig. 2c is the OCP of AC and PT samples in 1N HCl solution, the stabilized value of OCP exhibits negligible difference, indicating comparable thermodynamic corrosion stability [30]. However, from the potentiodynamic polarization curve shown in Fig. 2d, the PT sample has a higher self-corrosion potential (E_{corr}) and lower corrosion current density (I_{corr}), especially the significantly wider passivation zone (ΔE), indicating that PT could enhance the corrosion resistance of Zr-based MG, mainly reflected in reducing its corrosion tendency and forming a more stable passivation film. The surface micro-topography after potentiodynamic polarization treatment in Fig. S3 can confirm the above conclusions.

3.3. *Wear behavior and mechanism analysis in pure water*

Wear experiments in pure water conducted as a reference for subsequent experiments, as illustrated in Fig. 3a, the coefficient of friction (COF) curve of AC samples exhibited obvious fluctuations during the "running-in" stage, after entering the steady-state wear stage, the COF gradually stabilizes and increases. In contrast, Fig. 3c displays the PT samples have a similar upward trend but with minimal fluctuations during the "running-in" stage, yielding a lower average COF of 0.39, lower than the average COF of 0.46 of the AC sample. Fig. 3b–c revealed 3D morphology and cross-sectional profile of AC samples, wear tracks revealed severe material loss [31], with area of wear tracks S_1 of 307.9 μm^2 calculated by integrating the 3D profile, afterwards the wear rate ω_1 is 29.3 × 10^{-6} mm^3 N^{-1} m^{-1} was calculated by applying equation (1). Conversely, as shown in Fig. 3e–f, the PT samples exhibited negligible wear traces in 3D morphology, with area of wear tracks S_2 of 22.5 μm^2 and wear rate ω_2 of 2.14 × 10^{-6} mm^3 N^{-1} m^{-1}, which was only 7.3 % of the AC wear rate (ω_2/ω_1 = 0.073), demonstrating enhanced wear resistance under pure water conditions.

Fig. 4a displays the wear morphology of the AC sample under pure water lubrication, the obvious grooves reveal characteristics of abrasive wear [32]. Additionally, regions of plastic deformation are observed, where localized tribolayers formed under sustained loading suggest adhesive wear mechanisms [22]. A magnified view in Fig. 4b further reveals microcracks, delamination, and debris accumulation within the tribolayer, indicating the mechanism of fatigue wear [11]. Energy-dispersive spectroscopy (EDS) data of all spot analyses is shown

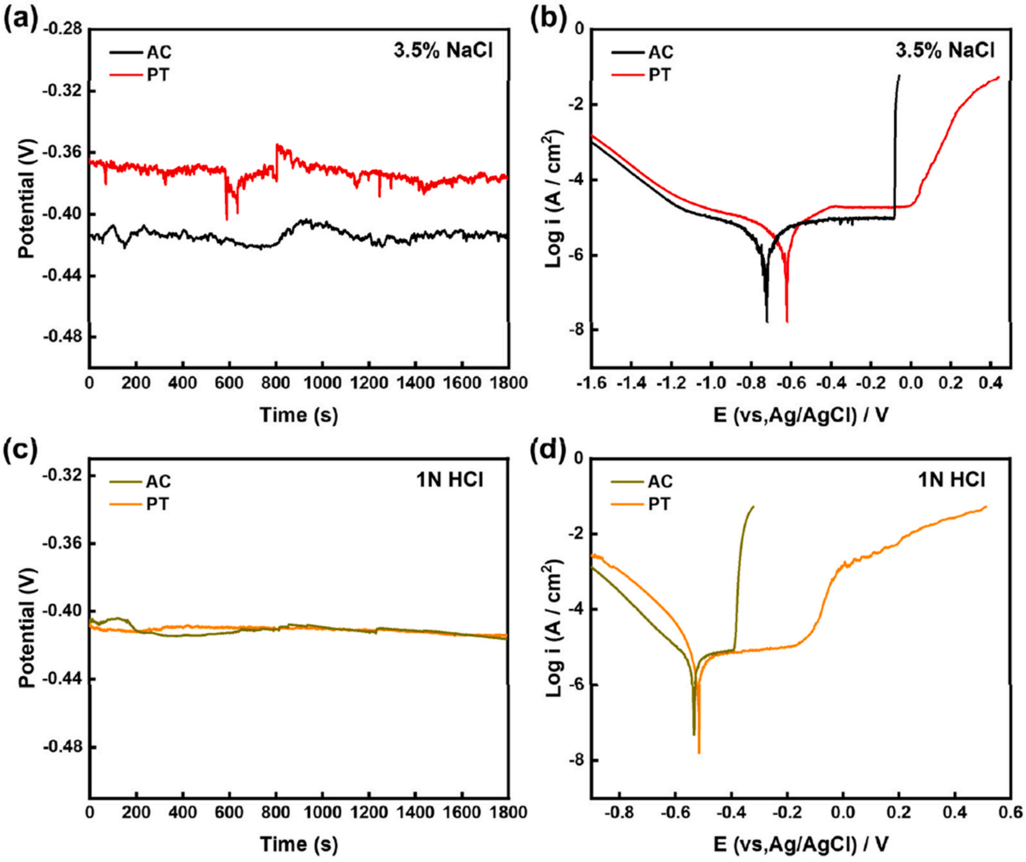

Fig. 2. (a) Open circuit potential (OCP) curves of AC and PT samples in 3.5 % NaCl solution. (b) Polarization curves of AC and PT samples in 3.5 % NaCl solution. (c) OCP curves of AC and PT samples in 1 N HCl solution. (d) Polarization curves of AC and PT samples in 1 N HCl solution.

Table 1
Electrochemical parameters of AC and PT samples in 3.5 % NaCl and 1N HCl solution.

Solution	Samples	E_{corr} (V)	I_{corr} (10^{-6} A/cm^2)	E_{nit} (V)	ΔE (V)
NaCl	AC	−0.741	1.708	0.081	0.556
	PT	−0.684	2.276	0.026	0.558
HCl	AC	−0.416	5.297	−0.389	0.096
	PT	−0.414	5.185	−0.127	0.355

in Table 2, the oxygen content of unworn surface P_1 and wear debris P_2 of the AC sample is 1.12 % and 51.15 % respectively, the significant differences demonstrates that, liquid cooling cannot fully suppress oxidation induced by frictional heating during prolonged friction in pure water, confirming a combined wear mechanism involving abrasive, adhesive, fatigue, and oxidative wear for the AC sample [33].

Fig. 4c presents the wear morphology of the PT sample, which exhibits narrower wear tracks and negligible surface damage. However, the magnified image in Fig. 4d reveals microcracks, voids, and spallation, indicating fatigue wear accumulation over extended sliding [34]. EDS analysis of the unworn region P_3 and fatigue-affected zone P_4 in Table 2 shows similar oxygen content of 48.55 % and 50.61 %, respectively, suggesting that liquid cooling effectively mitigates oxidation caused by frictional heating in the PT sample [35]. Thus, the wear mechanism of the PT sample in pure water is dominated by fatigue wear and minor oxidative contributions.

3.4. Wear behavior and mechanism analysis in 3.5 % NaCl solution

Fig. 5a presents the COF of the AC sample during wear in 3.5 % NaCl solution. Following an initial “running-in” stage, the COF exhibits a gradual increase with pronounced fluctuations, which may be attributed to the formation and detachment of corrosion products during corrosion-wear [36]. The average COF of 0.15 for the AC sample is significantly lower than the 0.46 COF measured in pure water, indicating superior lubrication performance of the NaCl solution [37]. 3D morphology and cross-sectional profile of the AC wear track in Fig. 5b–c reveal typical abrasive grooves, confirming abrasive wear as the dominant mechanism. The area of wear tracks S_3 is 312.4 μm^2, integrated from the 3D profile, yielding a wear rate ω_3 of 29.8×10^{-6} mm^3 N^{-1} m^{-1} using equation (1). Notably, the wear rate in NaCl solution remains comparable to that in pure water, suggesting that chloride ions do not exacerbate wear severity under neutral conditions [38].

Fig. 5d shows the COF curve for the PT sample, which exhibits smoother fluctuations and rapid transition to steady-state wear after the “running-in” stage. The higher COF of 0.21 compared to the AC sample may correlate with the formation of a lubricating tribocorrosion layer on the AC surface during corrosion-assisted wear [39]. The 3D topography of the wear track of the PT sample in Fig. 5e reveals a narrower scar width, indicating enhanced corrosion-wear resistance. Cross-sectional analysis shows in Fig. 5f yields an area of wear tracks S_4 of 16.3 μm^2 and a wear rate ω_4 of 1.55×10^{-6} mm^3 N^{-1} m^{-1}, confirming the substantial reduction in wear loss achieved by PT in NaCl environments.

Fig. 6a illustrates the wear morphology of the AC sample after wear test in 3.5 % NaCl solution, the distinct grooves indicate that the existence of abrasive wear. The high-magnification image in Fig. 6b highlights severely worn regions containing white particles and flake-like tribo-layer structures, suggesting a synergistic effect of corrosion and mechanical wear. Further magnification in Fig. 6c reveals film peeling and cracks within the tribo-layer, implying that the AC sample continuously forms new friction layers and fatigue falls off during the corrosion and wear [40], which is a signal of fatigue wear. Elemental analysis

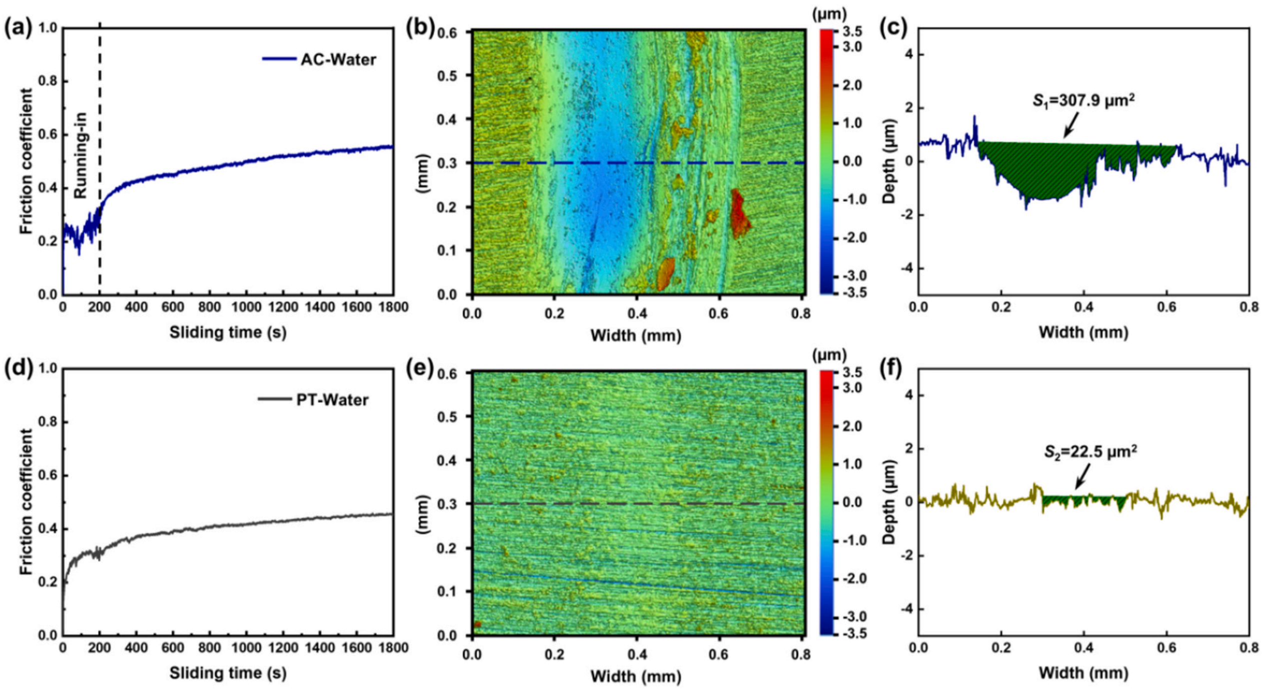

Fig. 3. (a) Coefficient of friction (COF) versus time curve of AC sample wear in pure water. (b) 3D wear morphology of the AC sample wear in pure water. (c) Cross-sectional profile of AC sample wear in pure water. (d) COF versus time curve of PT sample wear in pure water. (e) 3D wear morphology of the PT sample wear in pure water. (f) Cross-sectional profile of PT sample wear in pure water.

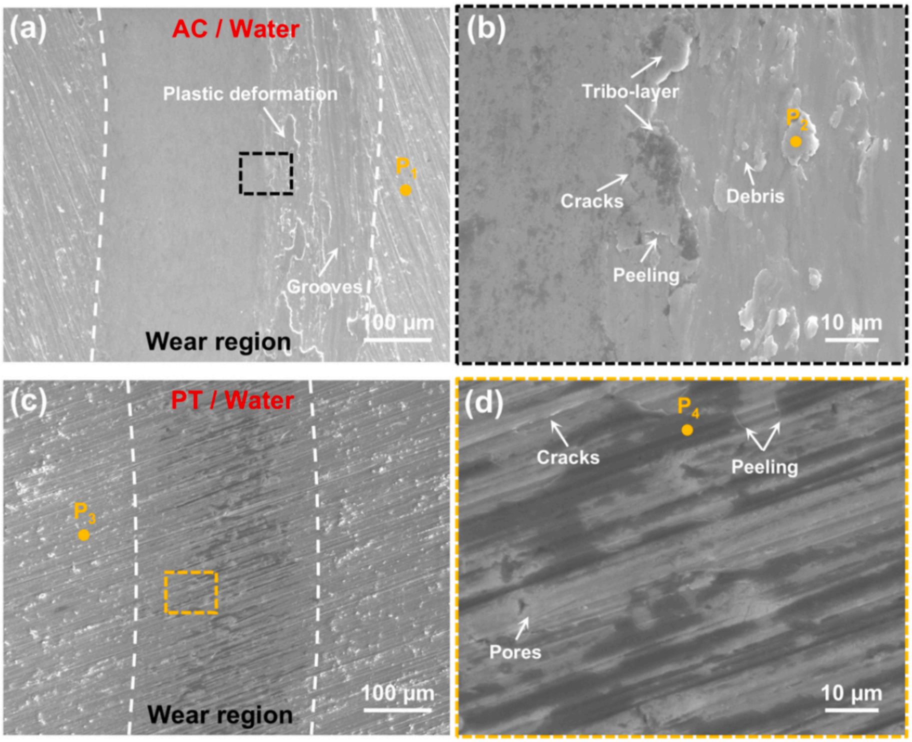

Fig. 4. (a)–(b) The wear morphology and magnification of AC sample after wear in pure water. (c)–(d) The wear morphology and magnification of the PT sample after wear in pure water.

of characteristic regions in Table 1 reveals an oxygen content of 4.87 % in the unworn region P_5, contrasting clearly with 52.58 % in the flake-like tribo-layer P_6, confirming the tribo-layer as a corrosion-wear synergistic product, the AC sample in NaCl solution inevitably experiences friction-induced oxidation like wear in pure water. The absence of pitting corrosion in the overall wear morphology is attributed to the superior repassivation capability of Zr-based MG in NaCl environments [41], when the friction layer falls off due to mechanical wear, the exposed substrate will quickly repassivate to form a corrosion-resistant passivation film. The dominant wear mechanisms of the AC sample in

Table 2
Statistical analysis of element content in different characteristic areas of wear marks of AC and PT sample.

	Element content (%)				
Position	Zr	Cu	Ni	Al	O
P_1	46.27	33.99	5.85	12.77	1.12
P_2	22.64	17.41	3.01	5.52	51.45
P_3	24.68	17.08	3.02	6.67	48.55
P_4	24.01	15.83	2.92	6.63	50.61
P_5	45.29	32.22	6.10	11.61	4.87
P_6	23.96	15.55	2.61	5.30	52.58
P_7	23.75	15.60	2.82	6.63	51.20
P_8	24.07	14.84	2.49	6.08	52.12
P_9	45.84	33.89	5.43	11.83	3.01
P_{10}	25.40	23.44	3.69	6.85	40.62
P_{11}	25.05	16.99	2.90	6.68	48.38
P_{12}	25.51	19.00	3.43	6.20	45.86

3.5 % NaCl solution are thus identified as corrosion-accompanied abrasive wear, adhesive wear, fatigue wear, and minor oxidative wear.

The wear morphology of the PT sample after wear in 3.5 % NaCl solution is depicted in Fig. 6d–f. Fig. 6d reveals an exceptionally smooth wear track with only slight abrasive wear features, magnified observation in Fig. 6e shows a relatively flat surface with debris and white-spot corrosion products derived from slight corrosion-wear. Higher-magnification Fig. 6f confirms localized clustering of white-spot products but absence of continuous tribo-layer, indicating that the corrosion and wear degree of PT samples in 3.5 % NaCl solution is relatively mild. This reduction is attributed to the mechanically hard oxide layer formed during PT, which effectively resists mechanical abrasion and initiates of corrosion. Elemental analysis in Table 2 demonstrates comparable oxygen contents of 51.20 % in the unworn substrate P_7 and 52.12 % in the debris-accumulated region P_8, suggesting that severe oxidative wear did not occur in the area of debris accumulation. Thus, the dominant wear mechanisms of the PT sample in 3.5 % NaCl solution are identified as slight abrasive wear and minor corrosion-wear. In comparison with the AC sample, the PT specimen exhibits superior corrosion-wear resistance, corroborating the efficacy of PT in enhancing the tribocorrosion durability of Zr-based MG in 3.5 % NaCl environments.

3.5. *Wear behavior and mechanism analysis in 1N HCl solution*

Fig. 7a depicts the COF evolution of the AC sample in 1N HCl solution, revealing an absence of a distinct “running-in” stage. Upon entering the steady-state wear, the COF exhibits obvious fluctuations with an average value of 0.02, these fluctuations are attributed to the frequent formation and exfoliation of corrosion-wear products in the highly corrosive environment, and these corrosion products have played a better lubricating role to a certain extent [42]. Fig. 7b–c presents the 3D morphology and cross-sectional profile of the wear track of AC sample, Fig. 7b reveals large scale grooves indicates severe abrasive wear happened during wear test. The cross-sectional area S_5 is 472.4 μm^2 yields a wear rate ω_5 of 44.99×10^{-6} mm^3 N^{-1} m^{-1}. This wear rate is significantly higher than those observed in pure water and 3.5 % NaCl solution, confirming the poorest corrosion-wear resistance of the AC sample in 1N HCl.

Fig. 7d demonstrates the COF curve of the PT sample in 1N HCl, which similarly lacks a “running-in” stage but exhibits more stable steady-state COF fluctuations compared to the AC sample, despite a slightly higher average COF of 0.04. This stability likely benefits from the superior corrosion-wear resistance of the PT sample, which reduces the frequency of corrosion product exfoliation. The 3D morphology wear track of PT sample in Fig. 7e confirms markedly reduced wear severity, the cross-sectional area S_6 is 9.26 μm^2 in Fig. 7f corresponding to a wear rate ω_6 of 0.88 × 10^{-6} mm^3 N^{-1} m^{-1}. The 50 times reduction in wear rate compared to the AC sample, proves the significant enhancement of corrosion-wear durability achieved by PT in strongly acidic chloride environments.

Fig. 8a displays the wear morphology of the AC sample worn in 1N HCl solution, reveals severe abrasive wear features which consistent with the 3D topography in Fig. 7b. Plastic flow deformation with significantly higher degree compared to the 3.5 % NaCl solution induced by corrosion-wear is evident, indicates aggravated corrosion-wear

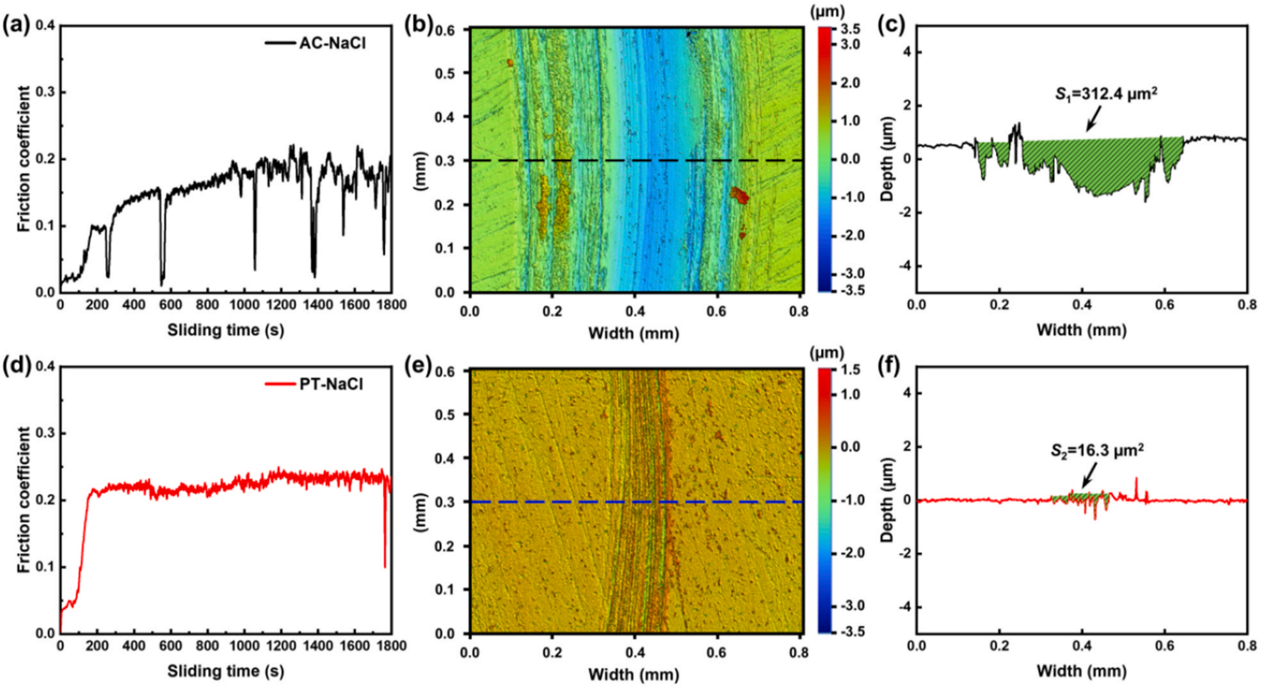

Fig. 5. (a) Coefficient of friction (COF) versus time curve of AC sample wear in 3.5 % NaCl solution. (b) 3D wear morphology of AC sample wear in 3.5 % NaCl solution. (c) Cross-sectional profile of AC sample wear in 3.5 % NaCl solution. (d) COF versus time curve of PT sample wear in 3.5 % NaCl solution. (e) 3D wear morphology of the PT sample wear in 3.5 % NaCl solution. (f) Cross-sectional profile of PT sample wear in 3.5 % NaCl solution.

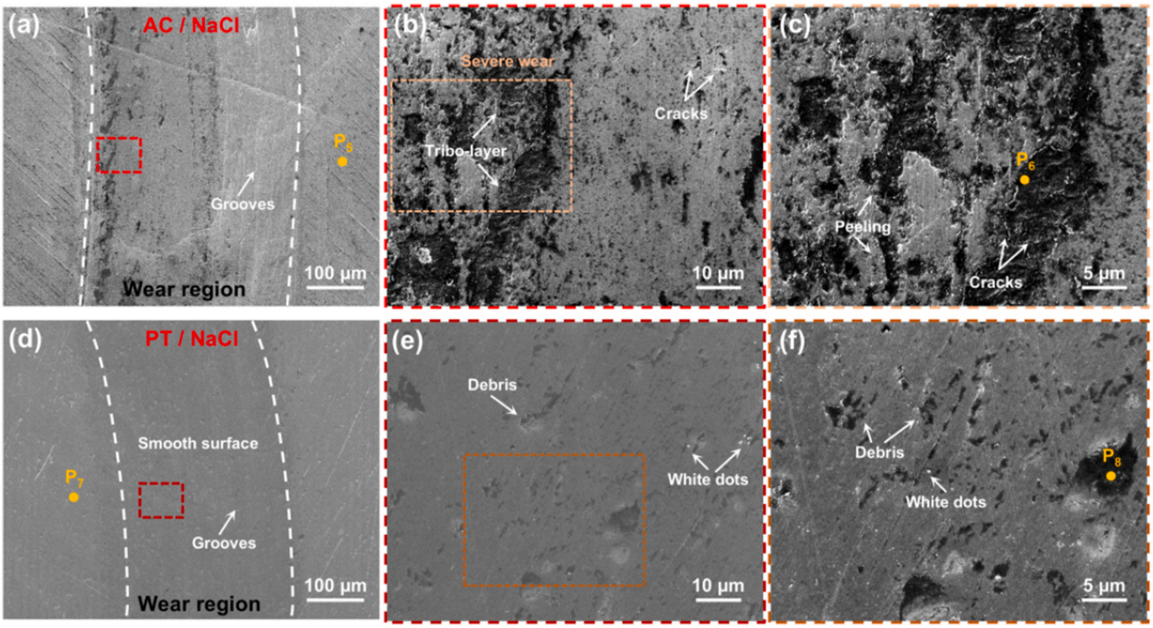

Fig. 6. (a)–(c) The wear morphology and magnification of the AC sample after wear in 3.5 % NaCl solution. (d)–(f) The wear morphology and magnification of the PT sample after wear in 3.5 % NaCl solution.

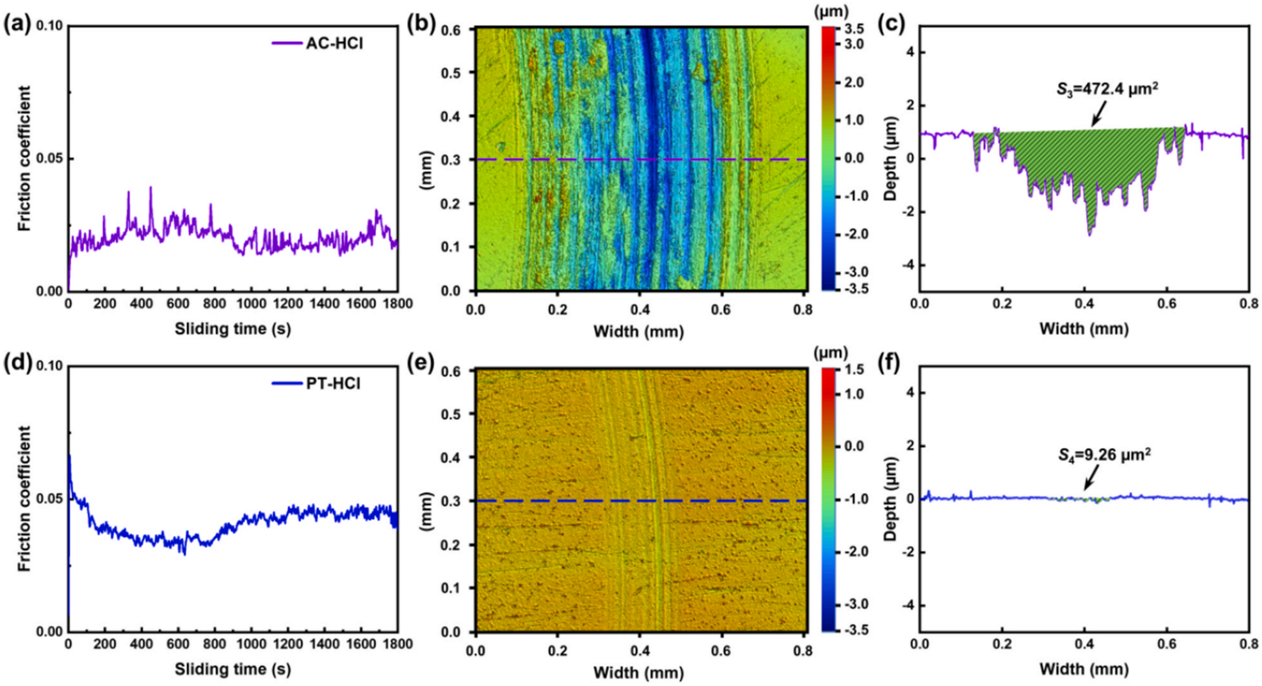

Fig. 7. (a) Coefficient of friction (COF) versus time curve of AC sample wear in 1 N HCl solution. (b) 3D wear morphology of AC sample wear in 1 N HCl solution. (c) Cross-sectional profile of AC sample wear in 1 N HCl solution. (d) COF versus time curve of PT sample wear in 1 N HCl solution. (e) 3D wear morphology of the PT sample wear in 1 N HCl solution. (f) Cross-sectional profile of PT sample wear in 1 N HCl solution.

damage in the acidic environment. The high-magnification Fig. 8b clearly shows the morphology of the tribo-layer and its peeling off, as well as slight pitting corrosion pits. The presence of these pits further confirmed the enhanced corrosion-wear severity in 1N HCl. At higher magnification of Fig. 8c, the cracking and peeling phenomenon of the tribo-layer is more obvious, which is due to the long-term mechanical wear and synergistic corrosion effect leading to crack propagation and gradual fatigue detachment. The oxygen content of the unworn substrate P_9 is 3.01 %, and the corrosion-worn film P_{10} is 40.62 %, significant oxygen enrichment in the damaged layer, ensuring the synergistic effect of corrosion and mechanical wear. Compared to the 3.5 % NaCl solution, the AC sample exhibits markedly intensified mechanical-corrosive synergism in 1N HCl, resulting in accelerated material loss [43]. The dominant wear mechanisms in 1N HCl are thus identified as severe corrosion-wear coupled with abrasive, adhesive, and fatigue wear, along with minor oxidative wear.

Fig. 8d presents the wear morphology of the PT sample in 1N HCl solution, revealing a narrower wear track compared to the AC sample,

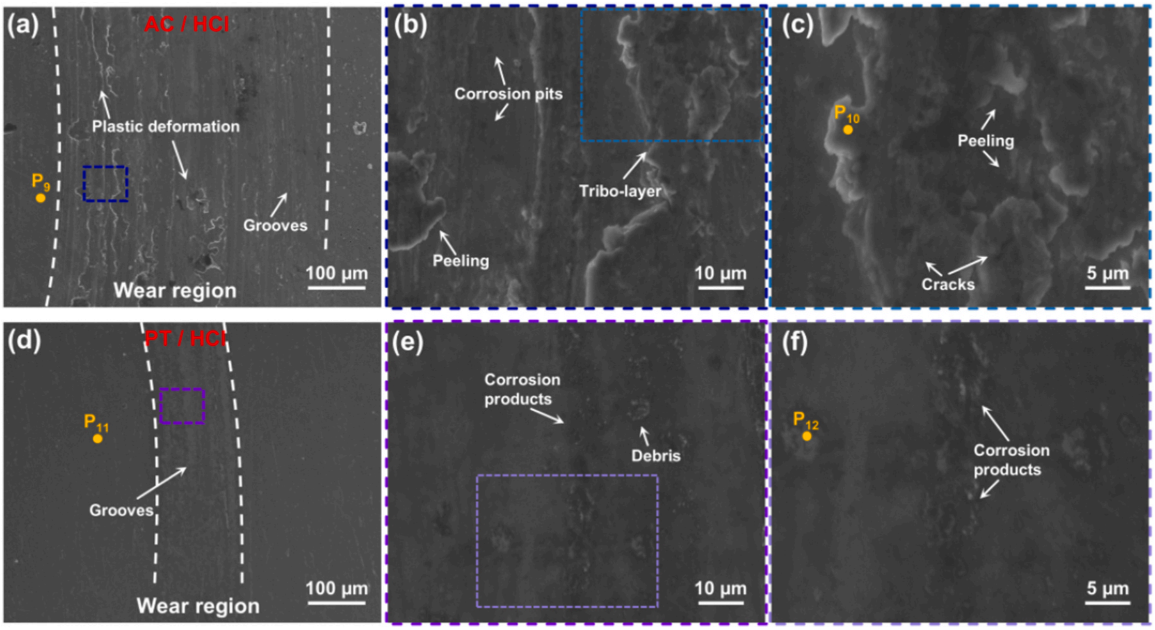

Fig. 8. (a)–(c) The wear morphology and magnification of the AC sample after wear in 1 N HCl solution. (d)–(f) The wear morphology and magnification of the PT sample after wear in 1 N HCl solution.

along with superficial grooves and adhered corrosion-wear debris, indicating concurrent abrasive and tribocorrosive damage. At higher magnification in Fig. 8d, aggregated corrosion-wear products and wear debris are clearly observable. The oxygen content of the unworn substrate P_{11} is 48.38 %, and the corrosion product layer P_{12} is 45.86 %, proving the comparable oxygen contents between the two regions. Although there are corrosion and wear products on the surface of the PT sample, its inherent excellent wear resistance makes the degree of corrosion and wear relatively mild [44]. Therefore, the wear mechanism of PT samples in 1N HCl solution is mild abrasive wear and corrosive wear.

3.6. Analysis of the mechanism for improved wear resistance by PT

Wear in corrosive solutions usually involves a synergistic effect of chemical corrosion and mechanical wear. On the one hand, mechanical wear may accelerate the chemical corrosion process, thereby increasing the corrosion rate; on the other hand, the presence of corrosive media may also exacerbate wear, resulting in more severe material wear losses than in an environment without corrosive media [45]. Generally speaking, the mass loss (m_T) caused by corrosive wear in materials is greater than the non-corrosive wear mass loss (m_W) and corrosive mass loss (m_C), with the excess being the synergistic effect mass (m_S) [46]. When the quality of the synergistic effect is positive, it indicates that the synergistic effect of corrosion and wear exacerbates the degree of material wear during the corrosion and wear process.

The above quality loss can be calculated using the following formula [47];

$$m_T = V_T \times \rho \tag{2}$$

$$m_W = V_W \times \rho \tag{3}$$

$$m_S = m_T - m_W - m_C \tag{4}$$

Where V_T is corrosion-wear volume loss (cm^3), V_W is non-corrosion wear volume loss (cm^3), ρ is density of materials (g/cm^3), here is 6.1 g/cm^3 in the Zr-based MG. According to the above formula, the synergistic effect mass of AC and PT samples in 3.5 % NaCl solution and 1N HCl solution was calculated separately. The specific data is summarized in Table 3, it can be seen that the synergistic effect mass of the AC sample in a strongly corrosive 1N HCl solution is positive, indicating that the synergistic effect of corrosion and mechanical wear in this solution exacerbates the degree of corrosion wear. In a 3.5 % NaCl neutral solution, the synergistic effect mass of the AC sample is 0, indicating that the degree of corrosion and wear did not further intensify in this solution. This is mainly attributed to the well repassivation ability of the AC samples in a 3.5 % NaCl solution, and its corrosion products lubricate the worn surface, thereby slowing down the synergistic destructive effect of corrosion and mechanical wear [17]. It is surprising that the synergistic effect mass of the PT sample in both 3.5 % NaCl solution and 1N HCl solution is negative, indicates that the corrosion and wear resistance of the material has not decreased two corrosive solutions, but increased.

In order to further investigate the reason behind the minimized synergistic effect of corrosion and wear on PT samples in corrosive HCl solution, X-ray photoelectron spectroscopy (XPS) analysis was conducted on the products of the worn surface of the PT sample in 1N HCl solution. Fig. 9 presents the characteristic peak spectra of major elements Zr 3d, Cu 2p, Al 2p, O 1s, and the C 1s as reference peak (BE = 284.8 eV) for charge correction. As shown in Fig. 9a, the Zr 3d spectrum exhibits two spin-orbit split peaks, $3d_5/_2$ at 182.4 eV and $3d_3/_2$ at 184.8 eV, predominantly assigned to Zr^{4+} in ZrO_2. The Cu 2p spectrum shown in Fig. 9b, displays two spin-orbit components $2p_1/_2$ and $2p_3/_2$, attributable to metallic Cu and its oxides. The Al 2p spectrum shown in Fig. 9c is dominated by peaks at 74.15 eV ($2p_3/_2$) and 76.51 eV ($2p_1/_2$), corresponding to Al_2O_3. The O 1s spectrum in Fig. 9d reveals two peaks at

Table 3
Quality loss statistics of AC and PT samples under different conditions.

Sample	Solution	Corrosive wear mass loss m_T (mg)	Non-corrosive wear mass loss m_W (mg)	Corrosive mass loss m_C (mg)	Synergistic effect mass m_S (mg)
AC	3.5 NaCl	0.588	0.578	0.01	0
	1N HCl	0.89	0.578	0.05	0.262
PT	3.5 NaCl	0.031	0.041	0.01	−0.021
	1N HCl	0.017	0.042	0.03	−0.055

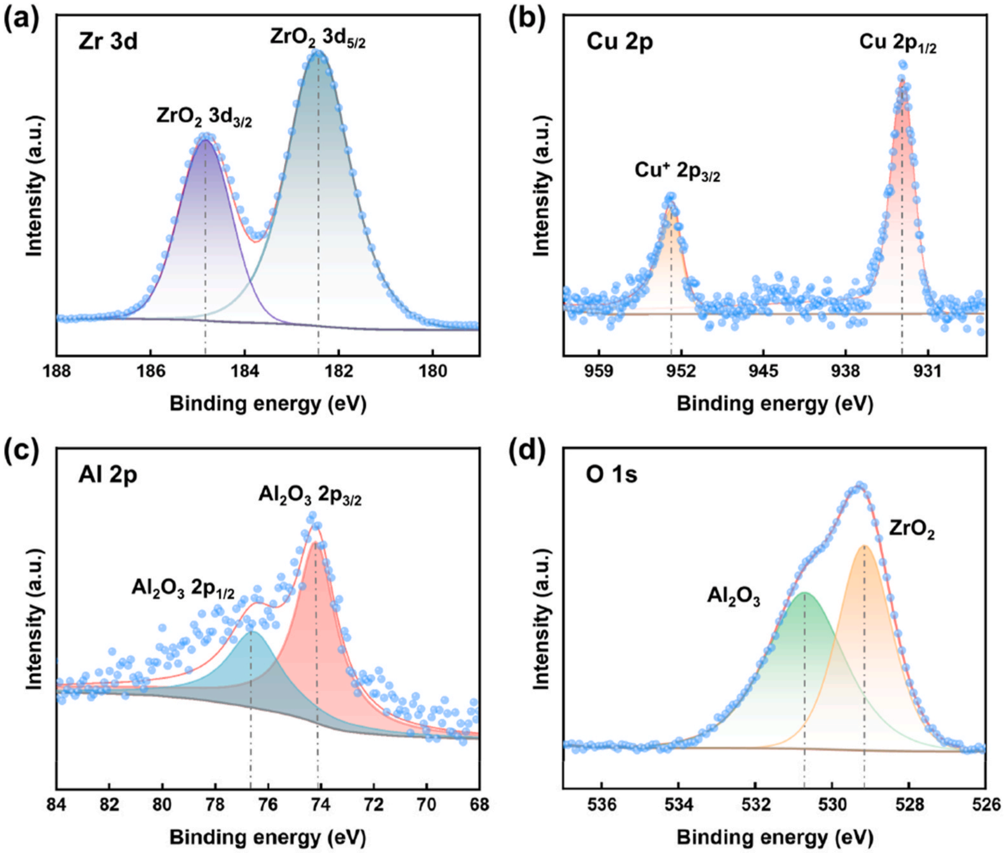

Fig. 9. XPS spectra of the worn surface of PT samples in 1 N HCl solution. (a) Characteristic spectra of Zr 3d. (b) Characteristic spectra of Cu 2p. (c) Characteristic spectra of Al 2p. (d) Characteristic spectra of O 1s.

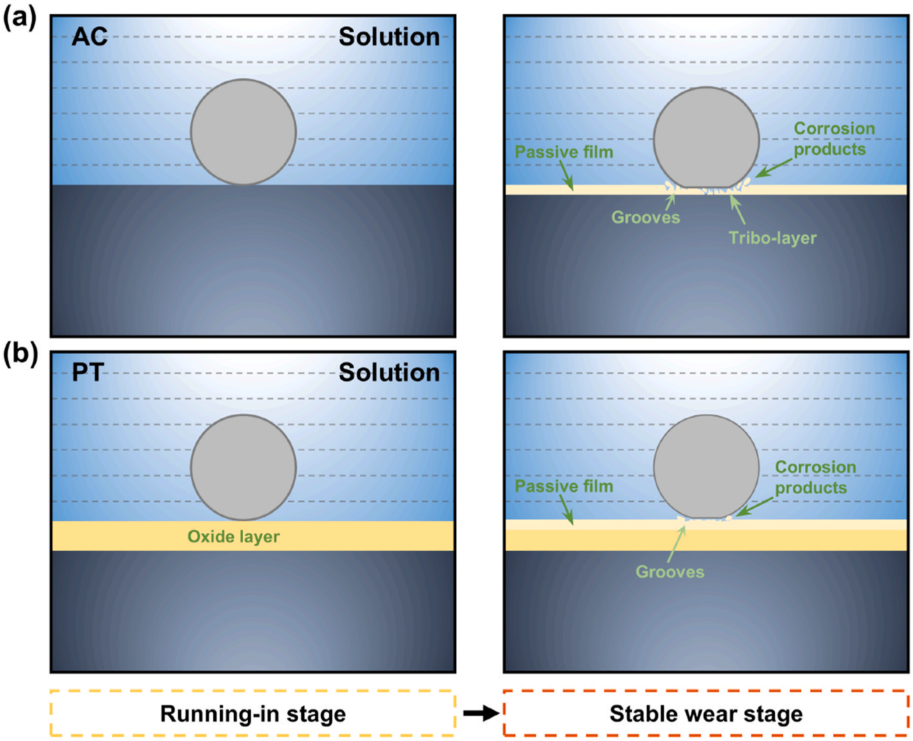

Fig. 10. (a) Wear mechanism diagram of AC sample in corrosive solution. (b) Wear mechanism diagram of PT sample in corrosive solution.

529.15 eV and 530.7 eV, assigned to lattice oxygen in ZrO_2 and Al_2O_3, respectively.

XPS analysis confirms the formation of a ZrO_2 and Al_2O_3 dominated passive film and corrosion-wear products on the surface of the wear track. In chloride-rich solutions, chloride ions compromise the stability and compactness of the passive film, resulting in softened wear debris and corrosion products [48]. The minimal synergistic corrosion-wear effect on the PT sample in 1N HCl can be attributed to two mechanisms, one is the softened wear debris and corrosion products act as lubricants during friction, reducing abrasive damage under high chloride ions concentrations, another is the pre-oxidized surface layer exhibits superior mechanical integrity, enhancing resistance to mechanical wear and thereby mitigating overall material loss [49].

Above all, in both 3.5 % NaCl and 1N HCl solutions, passive films are formed on Zr-based MG during wear to resist the synergistic destructive effect of corrosion and wear. As illustrated in the schematic wear mechanism diagram in Fig. 10a, a passive film formed on the AC sample, under the synergistic effect of corrosion and friction, the passivation film acts as a friction layer that gradually generates fatigue cracks and eventually peels off. But the debris and wear corrosion products formed during this process have a certain lubricating effect, thereby reducing the degree of wear. In contrast, the PT sample illustrated in Fig. 10b exhibits a hard surface oxide layer, which improves mechanical wear resistance. Furthermore, the generated corrosion-wear products in chloride-containing corrosive media serve as additional lubricants, further reducing wear. Consequently, pre-oxidized Zr-based BMGs effectively mitigate synergistic corrosion-wear damage, thereby enhancing their corrosion-wear resistance in both 3.5 % NaCl and 1N HCl solutions.

4. Conclusion

This study systematically investigated the impact of pre-oxidation treatment (PT) on the corrosion-wear behavior of Zr-based bulk metallic glasses (BMGs), focusing on the $Zr_{55}Cu_{30}Ni_5Al_{10}$ alloy. The electrochemical corrosion and corrosion-wear behaviors of AC and PT samples were examined in 3.5 % NaCl and 1N HCl solutions, alongside pure water as a control medium to elucidate the influence of corrosive environments on wear mechanisms. Electrochemical results revealed that PT substantially enhanced the corrosion resistance of Zr-based BMGs in both solutions: in 3.5 % NaCl, it improved thermodynamic stability and reduced corrosion susceptibility, while in 1N HCl, pre-oxidized samples exhibited higher corrosion potentials, lower current densities, and broader passivation ranges, indicating suppressed corrosion tendencies and the formation of more stable passive films.

In 3.5 % NaCl, the wear rates of AC and PT samples were 29.8×10^{-6} mm^3 N^{-1} m^{-1} and 1.55×10^{-6} mm^3 N^{-1} m^{-1}, respectively, demonstrates that PT significantly enhanced corrosion-wear resistance. Specifically, the AC sample underwent abrasive, adhesive, fatigue, and mild oxidative wear coupled with corrosion-wear, whereas the PT sample, with its harder surface oxide layer, resisted mechanical wear more effectively, reducing synergistic damage and primarily experiencing mild abrasive and corrosion-wear mechanisms. In the more aggressive 1N HCl solution, PT similarly improved corrosion-wear resistance, with the wear rate being ~50 times lower than that of the AC sample. These findings confirms that pre-oxidation effectively mitigates synergistic corrosion-wear damage in both neutral and acidic chloride-containing media by enhancing passive film stability and mechanical integrity.

CRediT authorship contribution statement

Yu Zhang: Validation, Formal analysis, Visualization, Investigation, Writing – original draft, Methodology, Data curation. **Wenxue Wang:** Formal analysis, Validation, Writing – review & editing. **Yong Xiao:** Conceptualization, Methodology, Validation. **Jiang Ma:** Supervision, Funding acquisition, Validation, Project administration, Writing – review & editing, Resources.

Data availability statement

All data needed to make the conclusions in the paper are present in the paper. Additional data related to this paper can be requested from the authors.

Declaration of competing interest

The authors declare that they have no known competing financial interests or personal relationships that could have appeared to influence the work reported in this paper.

Acknowledgments

The work was financially supported by the Science and Technology Innovation Commission Shenzhen (Grants No. RCJC20221008092730037 and 20220804091920001), the Key-Area Research and Development Program of Guangdong Province (Grant No. 2024B0101070001), the Research Team Cultivation Program of Shenzhen University (Grant No. 2023QNT001). We thank the Instrumental Analysis Center of Shenzhen University for the assistance with the electron microscope.

Appendix A. Supplementary data

Supplementary data to this article can be found online at https://doi.org/10.1016/j.intermet.2025.108897.

Data availability

Data will be made available on request.

References

[1] W. Klement, R.H. Willens, P.O.L. Duwez, Non-crystalline structure in solidified gold–silicon alloys, Nature 187 (1960) 869–870, https://doi.org/10.1038/187869b0.

[2] J. Ma, C. Yang, X. Liu, B. Shang, Q. He, F. Li, T. Wang, D. Wei, X. Liang, X. Wu, Y. Wang, F. Gong, P. Guan, W. Wang, Y. Yang, Fast surface dynamics enabled cold joining of metallic glasses, Sci. Adv. 5 (2019) eaax7256, https://doi.org/10.1126/sciadv.aax7256.

[3] H.B. Yu, Y. Luo, K. Samwer, Ultrastable metallic glass, Adv. Mater. 25 (2013) 5904–5908, https://doi.org/10.1002/adma.201302700.

[4] J. Das, M.B. Tang, K.B. Kim, R. Theissmann, F. Baier, W.H. Wang, J. Eckert, "Work-Hardenable" ductile bulk metallic glass, Phys. Rev. Lett. 94 (2005), https://doi.org/10.1103/PhysRevLett.94.205501.

[5] L. Tian, Y.-Q. Cheng, Z.-W. Shan, J. Li, C.-C. Wang, X.-D. Han, J. Sun, E. Ma, Approaching the ideal elastic limit of metallic glasses, Nat. Commun. 3 (2012), https://doi.org/10.1038/ncomms1619.

[6] M.M. Trexler, N.N. Thadhani, Mechanical properties of bulk metallic glasses, Prog. Mater. Sci. 55 (2010) 759–839, https://doi.org/10.1016/j.pmatsci.2010.04.002.

[7] L. Li, X. Li, Z. Huang, J. Huang, Z. Liu, J. Fu, W. Wen, Y. Zhang, S. Huang, S. Ren, J. Ma, Joining of metallic glasses in liquid via ultrasonic vibrations, Nat. Commun. 14 (2023), https://doi.org/10.1038/s41467-023-42014-x.

[8] Y.C. Hu, C. Sun, C. Sun, Functional applications of metallic glasses in electrocatalysis, ChemCatChem 11 (2019) 2401–2414, https://doi.org/10.1002/cctc.201900293.

[9] S.V. Madge, A. Caron, R. Gralla, G. Wilde, S.K. Mishra, Novel W-based metallic glass with high hardness and wear resistance, Intermetallics 47 (2014) 6–10, https://doi.org/10.1016/j.intermet.2013.12.003.

[10] Q. Qiao, Z. Cai, J. Wang, Z. Li, S. Feng, Z.-Q. Song, L.-M. Wang, Effects of adding niobium on microstructures and mechanical properties of ((Zr40Ti40Ni20) 72Be28)100-Nb bulk metallic glasses, J. Non-Cryst. Solids 618 (2023) 122529, https://doi.org/10.1016/j.jnoncrysol.2023.122529.

[11] Y. Zhang, Y.F. Ji, D.Q. Zhao, Y.X. Zhuang, R.J. Wang, M.X. Pan, Y.D. Dong, W. H. Wang, Glass forming ability and properties of Zr/nb-Based bulk metallic glasses, Scr. Mater. 44 (2001) 1107–1112, https://doi.org/10.1016/S1359-6462(00)00707-7.

[12] A. Inoue, A. Takeuchi, Recent development and application products of bulk glassy alloys, Acta Mater. 59 (2011) 2243–2267, https://doi.org/10.1016/j.actamat.2010.11.027.

[13] Y. Zhang, S. Sohrabi, X. Li, S. Ren, J. Ma, Tailored gradient nanocrystallization in bulk metallic glass via ultrasonic vibrations, J. Mater. Sci. Technol. 210 (2025) 109–120, https://doi.org/10.1016/j.jmst.2024.05.027.

[14] S. Sohrabi, J. Fu, L. Li, Y. Zhang, X. Li, F. Sun, J. Ma, W.H. Wang, Manufacturing of metallic glass components: processes, structures and properties, Prog. Mater. Sci. 144 (2024) 101283, https://doi.org/10.1016/j.pmatsci.2024.101283.

[15] X. Li, J. Fu, J. Sun, K. Song, J. Ma, Ultrasonic welding of metallic glasses: a review, Sci. China Mater., https://doi.org/10.1007/s40843-025-3302-4.

[16] X. Ji, H. Wang, Y. Bao, D. Zheng, Wear resistance of CuZr-based amorphous-forming alloys against bearing steel in 3.5% NaCl solution, Philos. Mag. 97 (2017) 3042–3054, https://doi.org/10.1080/14786435.2017.1364440.

[17] Y. Wang, L.-l. Shi, D.-l. Duan, S. Li, J. Xu, Tribological properties of Zr61Ti2Cu25Al12 bulk metallic glass under simulated physiological conditions, Mater. Sci. Eng. C 37 (2014) 292–304, https://doi.org/10.1016/j.msec.2014.01.016.

[18] M. Zhang, D. Yao, Z. Cao, P. Li, P. Zhou, X. Wang, Influence of oxidation on the performance of Zr55Cu30Al10Ni5 BMG, Intermetallics 79 (2016) 20–27, https://doi.org/10.1016/j.intermet.2016.08.007.

[19] R. Salehan, H.R. Shahverdi, R. Miresmaeili, Effects of annealing on the tribological behavior of Zr60Cu10Al15Ni15 bulk metallic glass, J. Non-Cryst. Solids 517 (2019) 127–136, https://doi.org/10.1016/j.jnoncrysol.2019.05.013.

[20] X.P. Nie, X.H. Yang, L.Y. Chen, K.B. Yeap, K.Y. Zeng, D. Li, J.S. Pan, X.D. Wang, Q. P. Cao, S.Q. Ding, J.Z. Jiang, The effect of oxidation on the corrosion resistance and mechanical properties of a Zr-based metallic glass, Corros. Sci. 53 (2011) 3557–3565, https://doi.org/10.1016/j.corsci.2011.06.032.

[21] F. Sun, S. Deng, J. Fu, J. Zhu, D. Liang, P. Wang, H. Zhao, F. Gong, J. Ma, Y. Liu, J. Shen, Superior high-temperature wear resistance of an ir-ta-ni-nb bulk metallic glass, J. Mater. Sci. Technol. 158 (2023) 121–132, https://doi.org/10.1016/j.jmst.2023.02.040.

[22] Y. Zou, Z. Qiu, Z. Zheng, G. Wang, X. Yan, S. Yin, M. Liu, D. Zeng, Ex-situ additively manufactured FeCrMoCB/Cu bulk metallic glass composite with well wear resistance, Tribol. Int. 162 (2021) 107112, https://doi.org/10.1016/j.triboint.2021.107112.

[23] W. Wang, F. Sun, H. Zhang, J. Huang, X. Yu, J. Ma, Improvement of high-temperature wear resistance of Zr-based metallic glass by pre-oxidation treatment, J. Mater. Res. Technol. 29 (2024) 2166–2174, https://doi.org/10.1016/j.jmrt.2024.01.169.

[24] Z. Tong, X. Pan, W. Zhou, Y. Yang, Y. Ye, D. Qian, X. Ren, Achieving excellent wear and corrosion properties in laser additive manufactured CrMnFeCoNi high-entropy alloy by laser shock peening, Surf. Coating. Technol. 422 (2021) 127504, https://doi.org/10.1016/j.surfcoat.2021.127504.

[25] L. Zhu, L. Li, J. Huang, H. Zhang, W. Wang, J. Chen, J. Liu, J. Ma, Corrosion resistance enhancement of bulk metallic glass through ultrasonic vibrations, J. Non-Cryst. Solids 646 (2024) 123223, https://doi.org/10.1016/j.jnoncrysol.2024.123223.

[26] N.C. Hosking, M.A. Ström, P.H. Shipway, C.D. Rudd, Corrosion resistance of zinc–magnesium coated steel, Corros. Sci. 49 (2007) 3669–3695, https://doi.org/10.1016/j.corsci.2007.03.032.

[27] Y. Okazaki, Y. Ito, K. Kyo, T. Tateishi, Corrosion resistance and corrosion fatigue strength of new titanium alloys for medical implants without V and Al, Mater. Sci. Eng., A 213 (1996) 138–147, https://doi.org/10.1016/0921-5093(96)10247-1.

[28] E. Budke, J. Krempel-Hesse, H. Maidhof, H. Schüssler, Decorative hard coatings with improved corrosion resistance, Surf. Coating. Technol. 112 (1999) 108–113, https://doi.org/10.1016/S0257-8972(98)00791-9.

[29] L. Peng, Y. Zhao, J. Ban, Y. Wang, P. Shen, J.-X. Lu, C.-S. Poon, Enhancing the corrosion resistance of recycled aggregate concrete by incorporating waste glass powder, Cement Concr. Compos. 137 (2023) 104909, https://doi.org/10.1016/j.cemconcomp.2022.104909.

[30] Z. Savaedi, H. Mirzadeh, R.M. Aghdam, R. Mahmudi, Effect of grain size on the mechanical properties and bio-corrosion resistance of pure magnesium, J. Mater. Res. Technol. 19 (2022) 3100–3109, https://doi.org/10.1016/j.jmrt.2022.06.048.

[31] X. Yan, H. Guo, W. Yang, S. Pang, Q. Wang, Y. Liu, P.K. Liaw, T. Zhang, Al0.3CrxFeCoNi high-entropy alloys with high corrosion resistance and good mechanical properties, J. Alloys Compd. 860 (2021) 158436, https://doi.org/10.1016/j.jallcom.2020.158436.

[32] X. Liu, X. Pei, Y. Du, Q. Zhou, H. Wang, Optimizing dry-wear performance of a Ti-based high entropy bulk metallic glass via isothermal annealing, J. Alloys Compd. 962 (2023) 171081, https://doi.org/10.1016/j.jallcom.2023.171081.

[33] C. Nyby, X. Guo, J.E. Saal, S.-C. Chien, A.Y. Gerard, H. Ke, T. Li, P. Lu, C. Oberdorfer, S. Sahu, S. Li, C.D. Taylor, W. Windl, J.R. Scully, G.S. Frankel, Electrochemical metrics for corrosion resistant alloys, Sci. Data 8 (2021) 58, https://doi.org/10.1038/s41597-021-00840-y.

[34] M. Sun, C. Du, Z. Liu, C. Liu, X. Li, Y. Wu, Fundamental understanding on the effect of Cr on corrosion resistance of weathering steel in simulated tropical marine atmosphere, Corros. Sci. 186 (2021) 109427, https://doi.org/10.1016/j.corsci.2021.109427.

[35] Z. Zhang, J. Yuan, G. Lian, S. Ren, Y. Du, R. Chen, W. You, R. Che, Nano FeCoNi-based high-entropy alloy for microwave absorbing with high magnetic loss and corrosion resistance, J. Alloys Compd. 988 (2024) 174175, https://doi.org/10.1016/j.jallcom.2024.174175.

[36] X. Liu, J. Bi, Z. Meng, R. Li, Y. Li, T. Zhang, Tribological behaviors of high-hardness Co-based amorphous coatings fabricated by laser cladding, Tribol. Int. 162 (2021) 107142, https://doi.org/10.1016/j.triboint.2021.107142.

[37] S. Li, P. Bai, Y. Li, W. Jia, X. Li, Y. Meng, L. Ma, Y. Tian, Extreme-pressure superlubricity of polymer solution enhanced with hydrated salt ions, Langmuir 36 (2020) 6765–6774, https://doi.org/10.1021/acs.langmuir.0c00887.

[38] M. Wang, T. Zander, X. Liu, C. Liu, A. Raj, D.C. Florian Wieland, V.M. Garamus, R. Willumeit-Römer, P.M. Claesson, A. Dėdinaitė, The effect of temperature on supported dipalmitoylphosphatidylcholine (DPPC) bilayers: structure and lubrication performance, J. Colloid Interface Sci. 445 (2015) 84–92, https://doi.org/10.1016/j.jcis.2014.12.042.

[39] D.D. Liang, X.S. Wei, T.C. Ma, B. Chen, H.R. Jiang, Y. Dong, J. Shen, Sliding tribocorrosion behavior of Fe-based bulk metallic glass under corrosive environments, J. Non-Cryst. Solids 510 (2019) 62–70, https://doi.org/10.1016/j.jnoncrysol.2018.12.024.

[40] X.-m. Zhang, W.-p. Chen, Review on corrosion-wear resistance performance of materials in molten aluminum and its alloys, Trans. Nonferrous Metals Soc. China 25 (2015) 1715–1731, https://doi.org/10.1016/S1003-6326(15)63777-3.

[41] P.F. Ji, B. Li, B.H. Chen, F. Wang, W. Ma, X.Y. Zhang, M.Z. Ma, R.P. Liu, Effect of Nb addition on the stability and biological corrosion resistance of Ti-Zr alloy passivation films, Corros. Sci. 170 (2020) 108696, https://doi.org/10.1016/j.corsci.2020.108696.

[42] P. Saha, M. Roy, M.K. Datta, B. Lee, P.N. Kumta, Effects of grain refinement on the biocorrosion and in vitro bioactivity of magnesium, Mater. Sci. Eng. C 57 (2015) 294–303, https://doi.org/10.1016/j.msec.2015.07.033.

[43] M. Herbster, K. Harnisch, P. Kriegel, A. Heyn, M. Krüger, C.H. Lohmann, J. Bertrand, T. Halle, Microstructural modification of TiAl6V4 alloy to avoid detrimental effects due to selective in vivo crevice corrosion, Materials 15 (2022) 5733, https://doi.org/10.3390/ma15165733.

[44] X. Hou, Y. Wang, L. Dai, Y. Yang, J. Du, Y. Wang, H. Wan, Study on the corrosion and wear behaviors of cylinder liner in marine diesel engine burning low sulfur fuel oil, Eng. Fail. Anal. 147 (2023) 107151, https://doi.org/10.1016/j.engfailanal.2023.107151.

[45] P. Jemmely, S. Mischler, D. Landolt, Electrochemical modeling of passivation phenomena in tribocorrosion, Wear 237 (2000) 63–76, https://doi.org/10.1016/S0043-1648(99)00314-2.

[46] S. Aribo, R. Barker, X. Hu, A. Neville, Erosion–corrosion behaviour of lean duplex stainless steels in 3.5% NaCl solution, Wear 302 (2013) 1602–1608, https://doi.org/10.1016/j.wear.2012.12.007.

[47] Y. Wang, Z.Z. Xing, Q. Luo, A. Rahman, J. Jiao, S.J. Qu, Y.G. Zheng, J. Shen, Corrosion and erosion–corrosion behaviour of activated combustion high-velocity air fuel sprayed Fe-based amorphous coatings in chloride-containing solutions, Corros. Sci. 98 (2015) 339–353, https://doi.org/10.1016/j.corsci.2015.05.044.

[48] R.Q. Guo, C. Zhang, Y. Yang, Y. Peng, L. Liu, Corrosion and wear resistance of a Fe-based amorphous coating in underground environment, Intermetallics 30 (2012) 94–99, https://doi.org/10.1016/j.intermet.2012.03.026.

[49] D.V. Louzguine-Luzgin, M. Ito, S.V. Ketov, A.S. Trifonov, J. Jiang, C.L. Chen, K. Nakajima, Exceptionally high nanoscale wear resistance of a Cu47Zr45Al8 metallic glass with native and artificially grown oxide, Intermetallics 93 (2018) 312–317, https://doi.org/10.1016/j.intermet.2017.10.011.